Supplemental Figures:

Fig. S1: FL-IRE1α-mNG cluster tracking and diffusion analysis in SNB-19 cells.

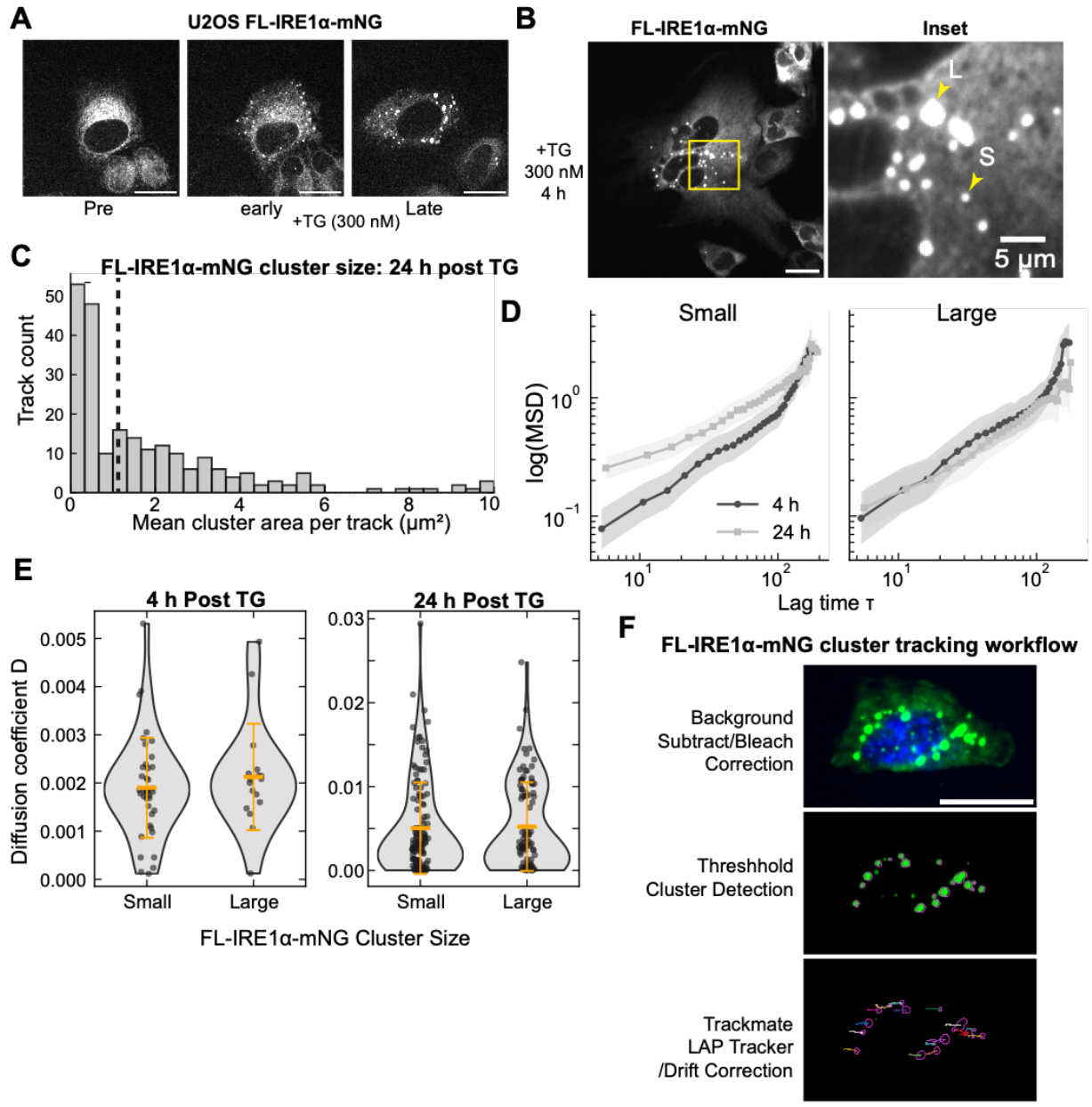

Figure S1: ***(A)*** *Representative confocal images of FL-IRE1α-mNG clusters in HEK293T, U2OS, EKVX, and SNB-19 cells following 300 nM TG treatment, illustrating cell-type differences in cluster growth and persistence. Scale bars, 20 µm.* ***(B)*** *Schematic showing the cluster area threshold used to define small (≤ 1.5 µm²) versus large (> 1.5 µm²) clusters for downstream MSD analysis.* ***(C)*** *Distribution of cluster areas at 24 h post-TG in SNB-19 cells, illustrating the bimodal size distribution and the threshold applied in B.* ***(D)*** *lag time vs log MSD plots of Small and Large clusters at ~4 h post TG vs 24 h post TG treatment.* ***(E)*** *Diffusion coefficient (D) of FL-IRE1α-mNG clusters binned by cluster area at 24 h post-TG, showing no significant size-dependent change in D, consistent with prior reports. Each point represents a single cluster track.* ***(F)*** *Schematic of cluster tracking process performed using Trackmate/LAP tracker.*

Fig. S2: Characterization of opto-IRE1α expression, phosphorylation, and signaling in HEK293T cells.

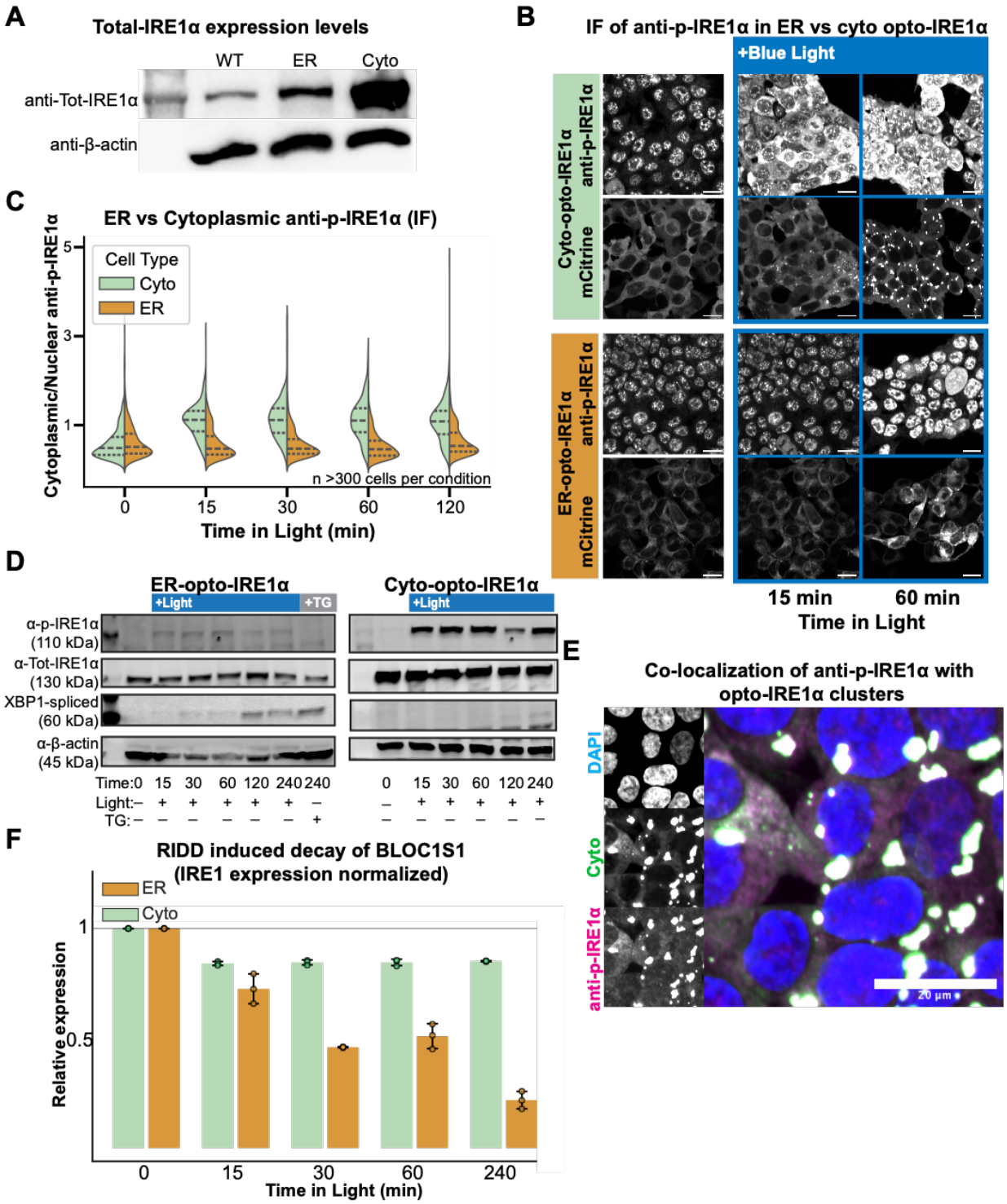

Figure S2: ***(A)*** *Western blot of whole-cell lysates from wild-type (WT), ER-opto-IRE1α, and Cyto-opto-IRE1α HEK293T cells probed with anti-total-IRE1α, showing that Cyto-opto-IRE1α requires ~4-fold higher expression than ER-opto-IRE1α for robust optogenetic clustering. β-actin is shown as a loading control.* ***(B)*** *Representative immunofluorescence images of HEK293T ER- and Cyto-opto-IRE1α cells stained with anti-p-IRE1α (S724) in dark conditions and after 240 min of illumination. mCitrine signal marks opto-IRE1α constructs. Scale bars, 20 μm.* ***(C)***

Quantification of cytoplasmic/nuclear mean fluorescence intensity ratio for anti-p-IRE1α (S724) over time in illuminated HEK293T ER- and Cyto-opto-IRE1α cells, showing elevated and sustained phosphorylation in Cyto-opto-IRE1α. Data shown are mean ± s.e.m.; n > 300 cells per time point. ***(D)*** *Time-course western blot of HEK293T ER- and Cyto-opto-IRE1α cell lysates probed for anti-p-IRE1α (S724), anti-total-IRE1α, anti-XBP1s, and anti-β-actin (loading control), confirming delayed XBP1s induction in Cyto-opto-IRE1α despite higher phosphorylation levels.* ***(E)*** *Representative immunofluorescence image of Cyto-opto-IRE1α cells co-stained with anti-p-IRE1α (S724) and imaged for mCitrine, demonstrating co-localization of phosphorylation signal with cytoplasmic clusters and confirming that hyperclusters are catalytically active. Scale bar, 20 μm.* ***(F)*** *qRT-PCR of the canonical RIDD substrate BLOC1S1 under actinomycin D-mediated transcriptional arrest in ER- and Cyto-opto-IRE1α cells at 0, 15, 30, 60, and 240 min of illumination. Values are normalized to total IRE1α expression levels. ER-opto-IRE1α drives more efficient BLOC1S1 decay per IRE1α molecule. Data shown are mean ± s.e.m. of n = 3 biological replicates.*

Fig. S3: Topology-dependent IRE1α signaling and growth arrest are recapitulated in U2OS cells.

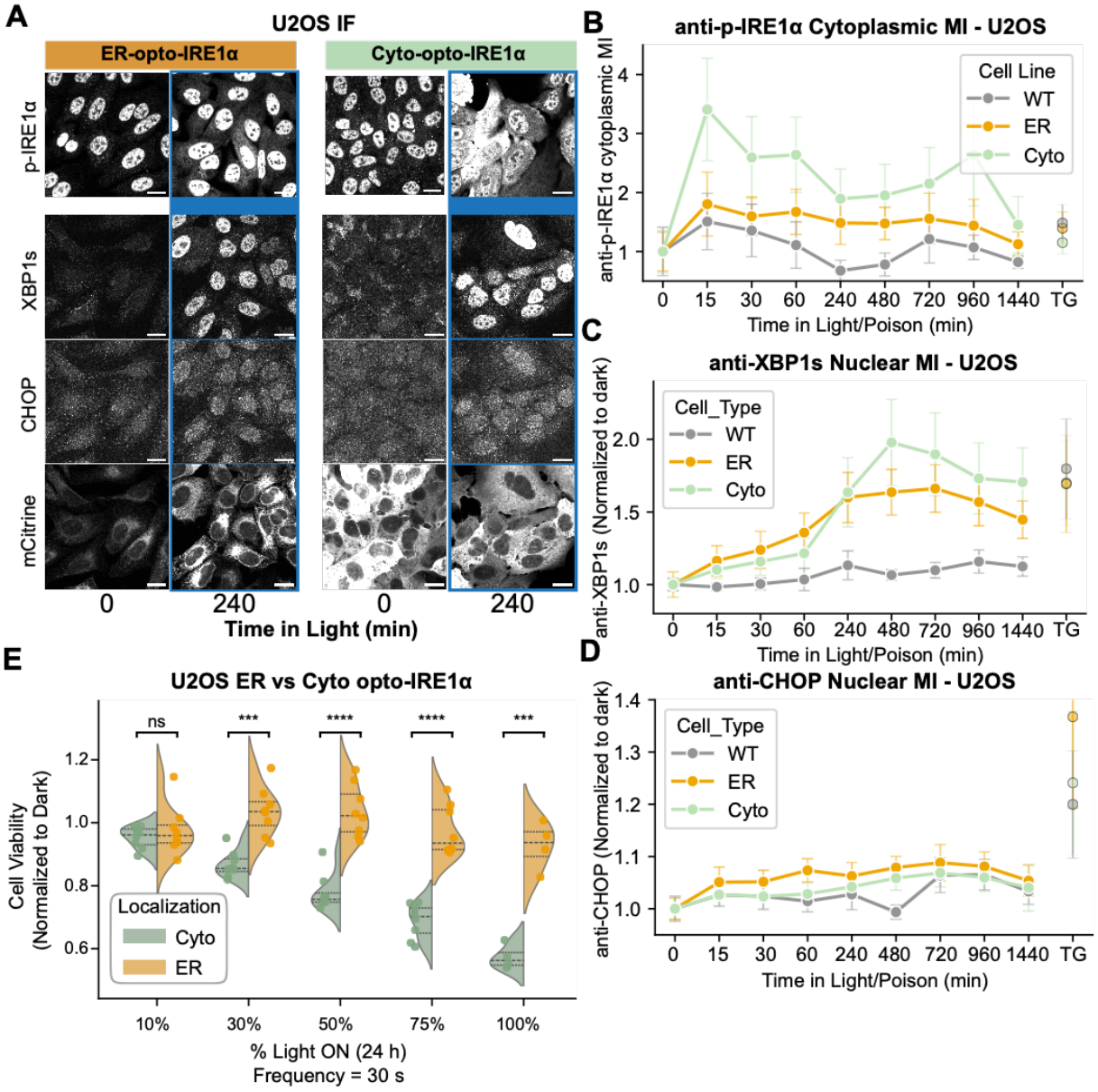

*Figure S3: **(A)** Representative immunofluorescence images of U2OS ER- and Cyto-opto-IRE1α cells stained for anti-XBP1s, anti-p-IRE1α (S724), and anti-CHOP after 240 min of illumination. 300 nM TG for 4 h serves as a positive control for CHOP induction. Scale bars, 20 µm. **(B-D),** Quantification of mean fluorescence intensity for anti-XBP1s (**B**), anti-p-IRE1α (S724) (**C**), and anti-CHOP (**D**) in U2OS ER- and Cyto-opto-IRE1α cells, normalized to respective dark controls. Positive control: 300 nM TG for 4 h. Data shown are mean ± s.e.m.; n ≥ 300 cells per condition. **(E)** Resazurin cell viability assay of U2OS ER- and Cyto-opto-IRE1α cells after 24 h of illumination at varying light duty cycles, normalized to dark controls. Growth arrest is observed selectively in Cyto-opto-IRE1α cells. Data shown are mean ± s.e.m.; n = 5 replicate wells. Independent t-test comparing ER versus Cyto at each duty cycle; ***p < 0.001, ****p < 0.0001.*

Fig. S4: Quality control and validation of the time-series bulk RNA-seq dataset.

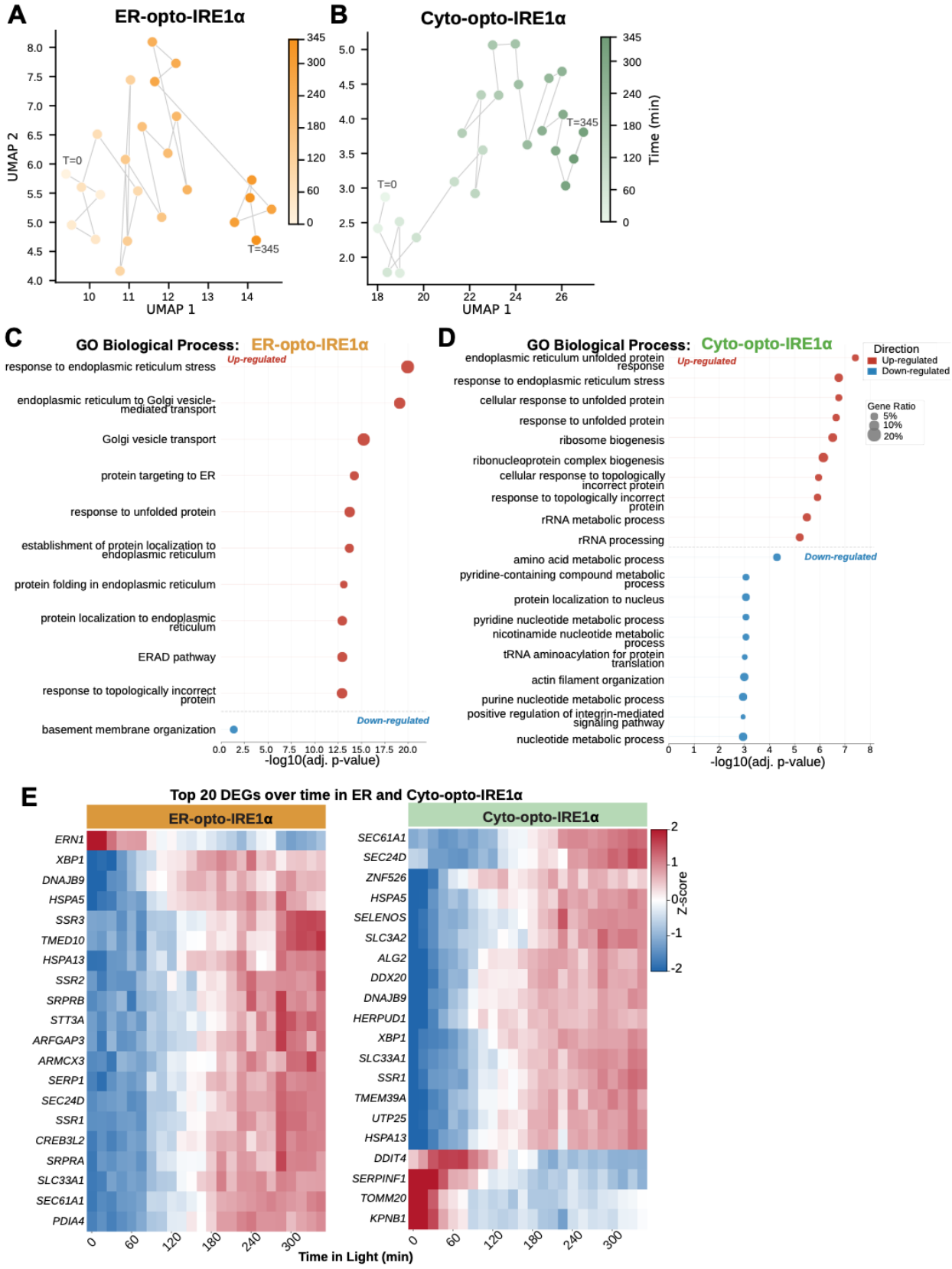

Figure S4: ***(A, B)*** *UMAP projections of all 48 RNA-seq samples (24 ER-opto-IRE1α and 24 Cyto-opto-IRE1α; 0–345 min, 15 min intervals). Samples cluster by both construct identity and time, confirming high sample quality and dynamic transcriptional responses.* ***(C, D)*** *Gene Ontology Biological Process enrichment for the top differentially expressed genes from DESeq2 analysis with spline fitting in ER-opto-IRE1α (**c**) and Cyto-opto-IRE1α (**d**) cells. Both conditions show enrichment for canonical ER stress response terms.* ***(E)*** *Z-scored heatmap of the top 20 DEGs (by adjusted p-value) for ER- and Cyto-opto-IRE1α across all time points, illustrating construct-specific gene activation patterns and validating that each optogenetic construct engages the expected IRE1α signaling program.*

Fig. S5: Cytoplasmic IRE1α drives topology-dependent transcript decay, spliceosome induction, and cell-cycle arrest without apoptosis.

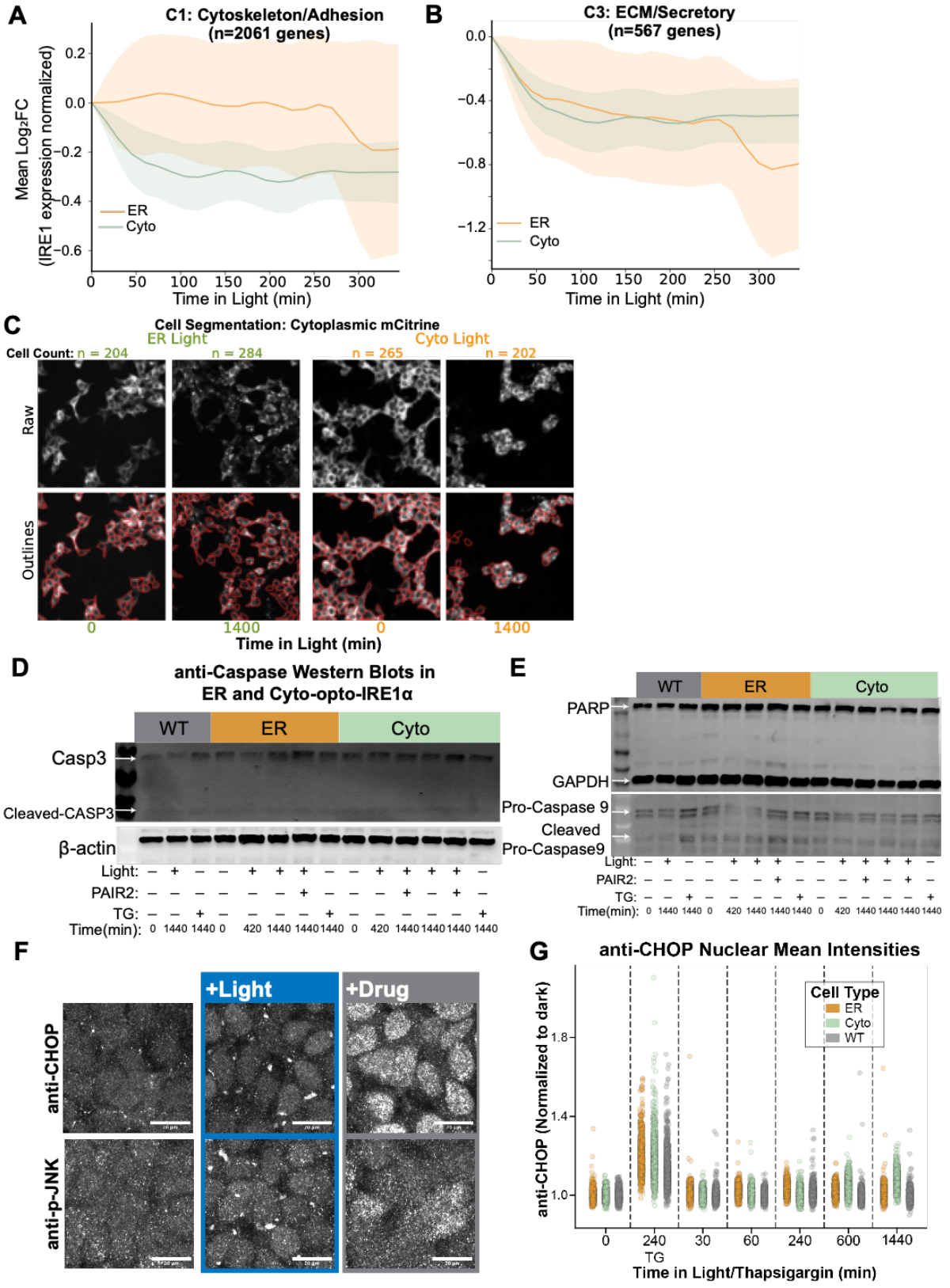

Figure S5: ***(A, B)*** *Mean log_2 fold change over illumination time for all genes in RNA-seq cluster C1 (cytoskeletal/adhesion, selectively decayed by Cyto-opto-IRE1α;* ***a****) and cluster C3 (canonical RIDD targets;* ***b****), with values scaled to total-IRE1α protein levels. After IRE1α expression normalization, C1 decay remains selective to Cyto-opto-IRE1α, whereas C3 decay is equivalent between constructs, confirming that the cytoskeletal decay program is topology-dependent rather than a dosage effect* ***(C)*** *Representative images of automated cell segmentation used for cell-count quantification in Fig. 3d, showing CellPose-derived masks for ER- and Cyto-opto-IRE1α cells at indicated time points.* ***(D, E)*** *Western blots for cleaved caspase-3 and procaspase-3 (****d****) and PARP and caspase-9 (****e****) in WT, ER-, and Cyto-opto-IRE1α HEK293T cells under dark conditions and after varying periods of illumination. No cleaved caspase-3, PARP cleavage, or caspase-9 activation is detected in illuminated cells. β-actin and GAPDH serve as loading controls, respectively.* ***(F)*** *Representative immunofluorescence images of HEK293T cells stained for anti-CHOP and anti-p-JNK after 240 min of illumination and after 240 min of 300 nM TG treatment. Neither ER- nor Cyto-opto-IRE1α illumination induces CHOP or p-JNK above background, whereas TG robustly activates both. Scale bars, 20 μm.* ***(G)*** *Quantification of nuclear anti-CHOP mean fluorescence intensity over illumination time in HEK293T cells, normalized to the mean of t = 0 min light. Data shown are mean ± s.e.m.; n ≥ 300 cells per time point.*

Fig. S6: XBP1-es is generated exclusively by cytoplasmic IRE1α and is detectable in human cancers.

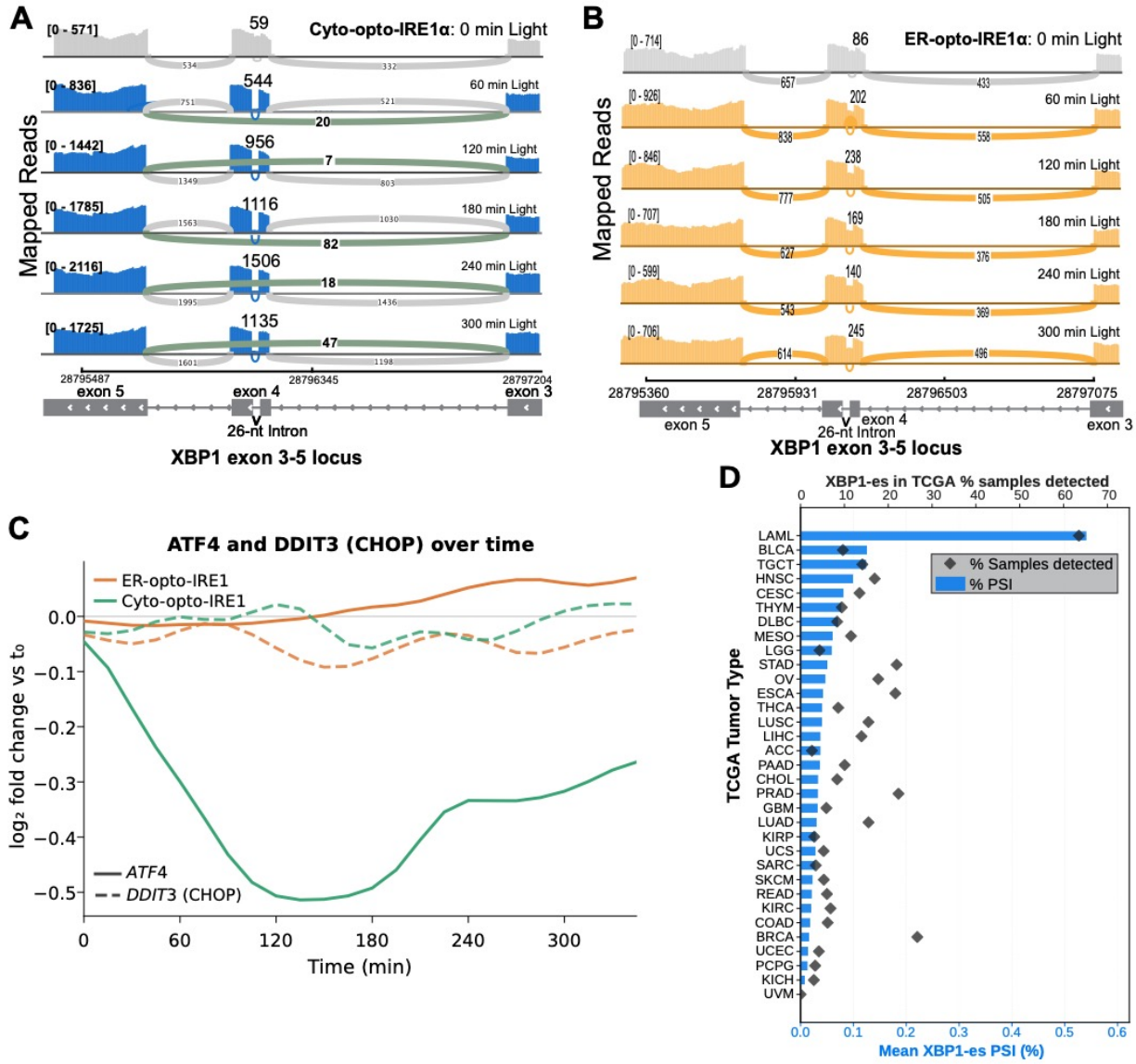

*Figure S6: **(A, B)** IGV sashimi plots of the XBP1 locus at six illumination time points (0, 60, 120, 180, 240, and 300 min) for ER-opto-IRE1α (**b**) and Cyto-opto-IRE1α (**a**) cells, showing junctions between exons 3–4, 4–5, and 3–5. Exon 3–5 junction reads (XBP1-es) are detectable in all illuminated Cyto-opto-IRE1α samples and absent from all ER-opto-IRE1α time points. **(C)** Expression of ATF4 and DDIT3/CHOP mRNA over illumination time in ER- and Cyto-opto-IRE1α cells, normalized to t = 0 min. **(D)** XBP1-es junction reads (exon 3–exon 5) detected in TCGA RNA-seq samples from 11,237 tumors via the Snaptron database (Snaptron TCGA v2 compilation, GRCh38). Percent Spliced In (PSI) for XBP1-es is shown across all cancer types with ≥ 5 supporting reads. Top x-axis = % samples detected, Bottom x-axis = % PSI in all tumors from a specific cancer.*

Fig. S7: XBP1-es retains broad UPR transcription factor activity but selectively fails to induce integrated stress response genes.

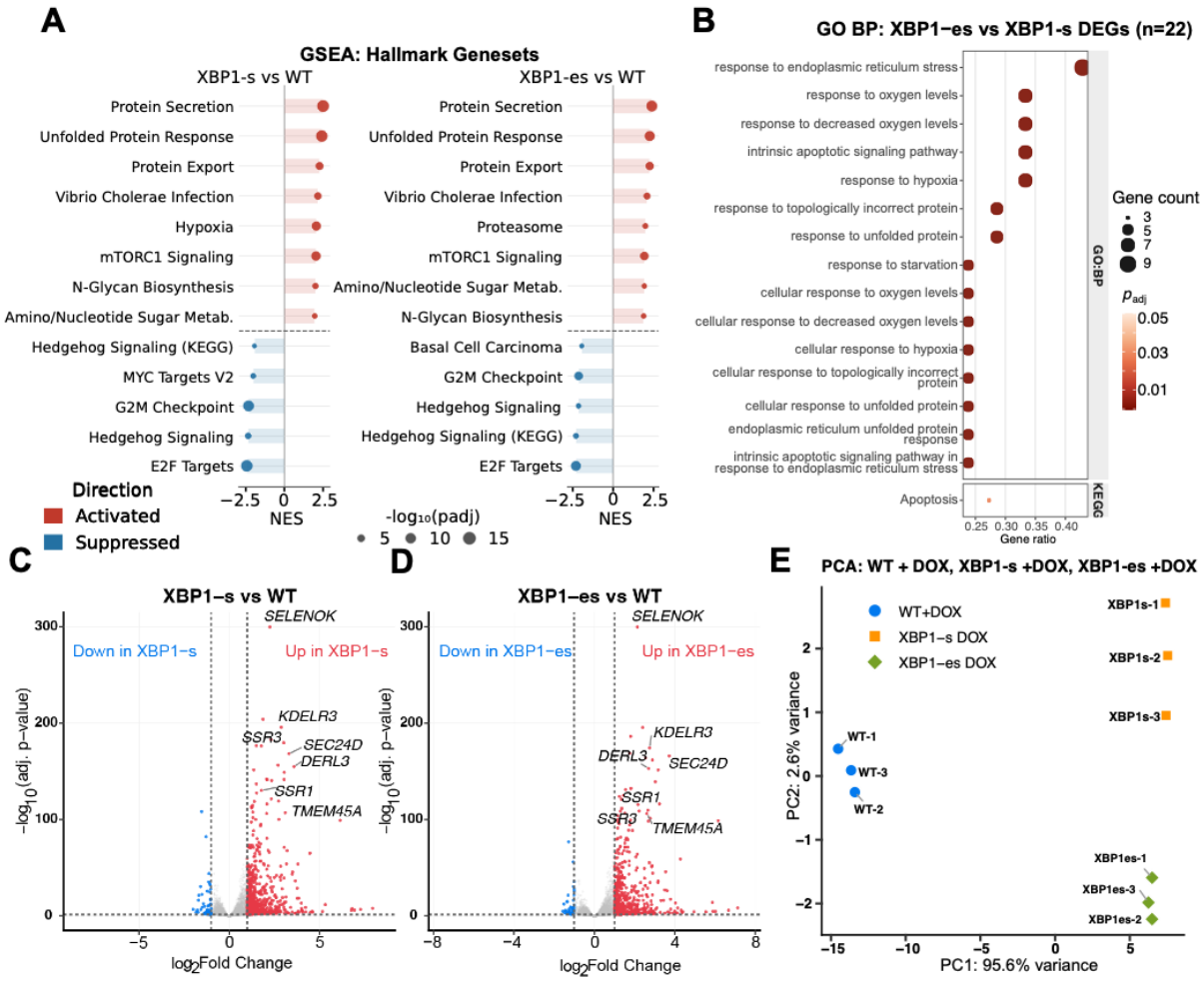

Figure S7: ***(A)*** *Gene Set Enrichment Analysis (GSEA) Hallmark pathway enrichment for doxycycline-induced XBP1-s versus wild-type and XBP1-es versus wild-type HEK293T cells (24 h doxycycline treatment; n = 3 biological replicates per condition). The top four upregulated Hallmark terms are identical between XBP1-s and XBP1-es, confirming broadly overlapping transcription factor activity.* ***(B)*** *Gene Ontology Biological Process enrichment for the 22 genes differentially expressed between XBP1-s and XBP1-es (adjusted $p < 0.05$, $|\log_2 FC| > 0.5$), showing enrichment for integrated stress response and ATF4-target gene sets.* ***(C, D)*** *Volcano plots of XBP1-s versus wild-type (c) and XBP1-es versus wild-type (d) comparisons. Differentially expressed genes are highlighted; genes uniquely upregulated in XBP1-s (including ATF4 and DDIT3/CHOP) are annotated. Adjusted p-values from DESeq2; dashed lines indicate $|\log_2 FC| = 1$ and adjusted $p = 0.05$ thresholds.* ***(E)*** *Principal component analysis (PCA) of all nine samples (n = 3 per condition: wild-type + doxycycline, XBP1-s + doxycycline, XBP1-es + doxycycline). PC1 accounts for 95.6% of total variance and separates wild-type from both XBP1 isoform-expressing samples; XBP1-s and XBP1-es samples are closely co-clustered, confirming the high similarity of their global transcriptional programs.*